10^7-A load-current *B*-dot monitor: Simulations, design, and performance

D. V. Rose, D. R. Welch, C. L. Miller, R. E. Clark, E. A. Madrid, and C. B. Mostrom
Voss Scientific, LLC, Albuquerque, New Mexico 87108, USA

T. C. Wagoner and J. K. Moore
Ktech Corporation, Albuquerque, New Mexico 87123, USA

W. A. Stygar, J. E. Bailey, T. J. Nash, G. A. Rochau, and D. B. Sinars
Sandia National Laboratories, Albuquerque, New Mexico 87185, USA
(Received 31 December 2009; published 21 April 2010)

A *B*-dot monitor that measures the current 6 cm from the axis of dynamic loads fielded on 10^7-A multiterawatt pulsed-power accelerators has been developed. The monitor improves upon the multimegampere load-current gauge described in Phys. Rev. ST Accel. Beams **11**, 100401 (2008). The design of the improved monitor was developed using three-dimensional particle-in-cell simulations that model vacuum electron flow in the transmission line near the monitor. The simulations include important geometric features of the *B*-dot probe and model the deposition of electron energy within the probe. The simulations show that the improved design reduces by as much as a factor of 5 the electron energy deposition to the interior of the monitor. Data taken on accelerator shots demonstrate that the improved monitor works as well as the original monitor on shots with low-impedance loads, and delivers superior performance on higher-impedance-load shots.

DOI: 10.1103/PhysRevSTAB.13.040401 PACS numbers: 52.58.Lq, 52.65.Rr, 84.70.+p

I. INTRODUCTION

Accurate determination of the current delivered to dynamic loads by large-scale pulsed-power accelerators is critical in understanding the performance of the accelerator-load system. The measurement of electrical currents delivered by the complex vacuum transmission line near the centrally located load on the 26-MA ZR accelerator [1–14] is particularly difficult due to dynamics of energetic electron flow in the evolving electromagnetic field.

B-dot probes that are used to measure currents in high-power transmission lines are often located in small cavities that are recessed behind the surfaces of the transmission-line electrodes [15]. The probes are recessed to prevent them from perturbing the performance of the transmission lines, shield the probes from electric fields in the lines, and in the case of magnetically insulated transmission lines (MITLs), shield the probes from electrons that flow in the lines. For a multiterawatt multimegajoule power pulse, shielding of the probes near a load is more difficult due to the high-energy-density environment [15]. Load-current measurements, such as those described in Ref. [15], are used to assess the performance of the accelerator-load system for a variety of load types, including *z*-pinches [16] and loads designed for isentropic-compression experiments [17–19].

The load-current *B*-dot probes on ZR are located 6 cm from the axis of the load, which is located at the center of the machine. Just upstream of these probes, electrical power that is transported by four radial MITLs is combined by a double-post-hole vacuum convolute [4,14,20–29]. The four MITLs located upstream of the convolute are referred to as the *outer* MITLs. The convolute delivers the combined power to a single MITL that drives the load. This single MITL, which connects the output of the convolute to the load, is referred to as the *inner* MITL.

It has long been recognized that electrons launched from the cathodes of the outer MITLs and convolute can reach the anode of the inner MITL. The original design of the inner-MITL *B*-dot probes used on the Z and ZR accelerators is described in Ref. [15]. These probes are located inside the convolute, which permits measurement of the total current delivered by the convolute to the inner MITL. The *B*-dot loop is recessed from the inner-MITL anode to keep the *B*-dot detector away from electrons that strike the anode. The *B*-dot loop is surrounded by copper to reduce penetration of magnetic flux into the walls of the *B*-dot-monitor aperture. (Such penetration changes the sensitivity of the monitor as a function of time.) In addition, the *B*-dot monitor is located at the same azimuthal location as one of the anode posts of the double-post convolute. The post is used to shield the *B*-dot from electrons that are launched upstream in the MITLs and convolute [4,14,23–28]. A more complete description of these monitors is given in Ref. [15].

The monitors described in this article are an improved version of the inner-MITL *B*-dot monitors discussed in Ref. [15]. The location of one of these monitors can be seen in Fig. 1, which illustrates ZR's four outer MITLs, double-post-hole convolute, and inner MITL. The drawing

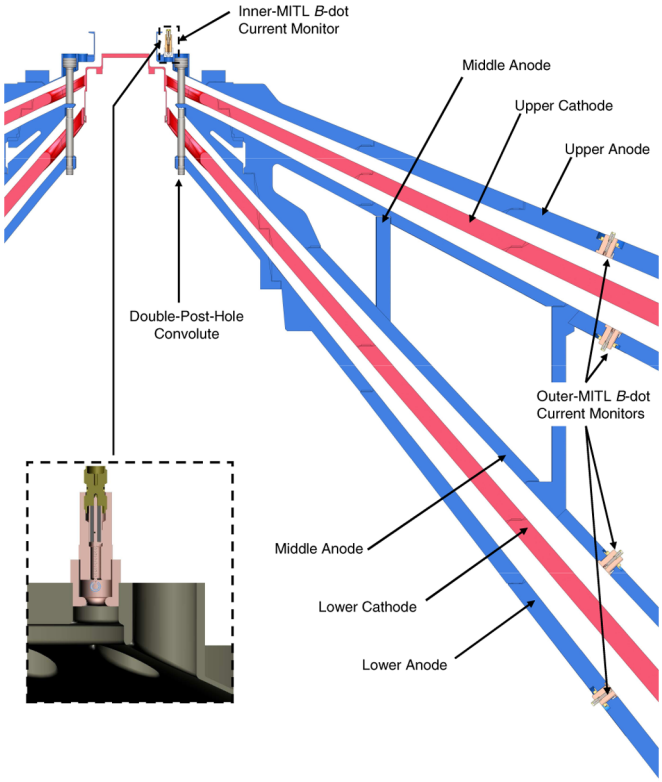

FIG. 1. (Color) Schematic of the ZR MITLs and double-post-hole convolute showing the locations of outer-MITL and inner-MITL current monitors. A detailed drawing of an inner-MITL monitor design is also shown.

shows the placement of the inner-MITL *B*-dot probe (upper left-hand corner of the figure) presently in use on ZR. Also shown are the locations of the four upstream outer-MITL monitors [15].

In this article, we describe 3D particle-in-cell (PIC) simulations that are used to model electron power flow in the vicinity of ZR's double-post-hole convolute during the rise time of the power pulse. The simulations include important geometric features of the existing ZR inner-MITL *B*-dot probes [15], and show electron energy deposition within the *B*-dot probe that is consistent with failure of the probe on relatively high-impedance-load shots. The simulation results have led to a redesign of the inner-MITL *B*-dot probes. The new probes have been fielded simultaneously with the original probes on recent ZR shots. The redesigned probes give current measurements through peak load power for shots with low-impedance loads (i.e., loads with an inductance of $\sim$3 nH at peak load voltage) that are in good agreement with measurements made with the original probes. In addition, the redesigned probes track the machine (total outer-MITL) current past the time of peak load power, an improvement over the performance of the original *B*-dot probes. For shots with higher-impedance loads (i.e., shots with an inductance of $\sim$5 nH at peak load voltage), the redesigned probes give load-current rise times that are more consistent with the machine current, provide more realistic load-current amplitudes through peak power, and track the machine current well past peak power. Overall, the redesigned *B*-dot probes have proven to be more robust to the deleterious effects of the dynamic electron power flow on ZR.

This paper mainly addresses electron impact at the monitor location prior to the onset of magnetic insulation of the electron flow as the total current flowing in the MITL increases. Other mechanisms can lead to failure of these types of probes, including the formation of dense electrode plasmas that can span the probe entrance aperture, soft x-ray and UV radiation bombardment of probe hardware (produced in the various load packages fielded on ZR), and direct electron pickup on the field-measuring wire loop. These topics are not treated in this work, but could, in principle, be modeled in the numerical simulations.

This paper is organized as follows. The 3D PIC simulation model of the ZR double-post-hole convolute and *B*-dot probe is described in Sec. II. The baseline *B*-dot probe design and two modifications are analyzed in Sec. III. A comparison of measured *B*-dot probe performance on several ZR dynamic-load shots is presented in Sec. IV. Section V provides a summary.

II. SIMULATION MODEL

The simulation model used here is similar to that described in Refs. [14,28]. The LSP PIC code [30] is used throughout in 3D (r, θ, z) coordinates. The simulations are fully electromagnetic, explicit, and use an energy-conserving cloud-in-cell model for the particles [31–33]. The cloud-in-cell model reduces numerical heating associated with under-resolution of the plasma Debye length and electrostatic fluctuations on the grid. The objective is to efficiently model electron dynamics in the convolute at early times in the power pulse, prior to the onset of magnetic insulation in the vicinity of the inner-MITL *B*-dot probes. To achieve this, the simulations are driven by a forward-going voltage pulse that gives a current rise time, dI/dt, of 200 kA/ns, which is approximately equal to the ZR load-current rate of rise for a shot with a nominal current rise time of 100 ns (i.e., a shot taken in ZR's short-pulse operating mode). At this value of dI/dt, magnetic insulation occurs in the simulations within 30 ns of the beginning of the power pulse.

The basic simulation geometry is illustrated by Fig. 2 and represents the standard 12-post ZR convolute [4,14]. Power enters the PIC simulation through four inlets located at a radius of 14 cm. The load is modeled as an idealized cylindrical imploding liner with a 2-cm initial radius. The load inductance is time dependent and is calculated assuming a simple single-shell, snow-plow model [28]. On the short time scales used for the present simulations, the load dynamics are not important and the load model is used only to provide the approximate time-dependent inductance of the load at the simulation outlet boundary.

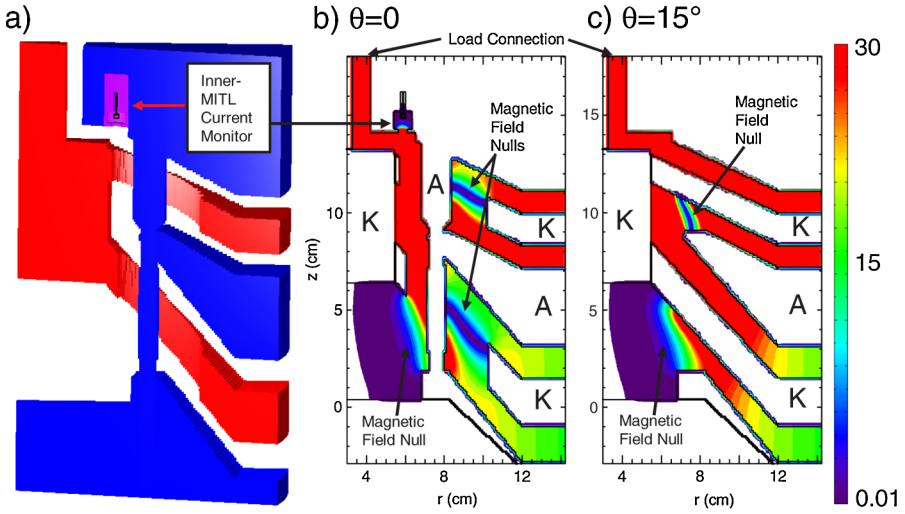

FIG. 2. (Color) ZR convolute simulation geometry used for evaluating inner-MITL current probe designs. (a) 3D rendering of the entire simulation space with cathode parts in blue, anode parts in red. Magnetic field amplitude contours (in kG) at $t = 45$ ns in the (b) $\theta = 0$ and (c) $\theta = 15$ deg simulation planes. Anode (A) and cathode (K) parts are labeled as well as the locations of the magnetic field nulls.

Current bifurcations within the double-post-hole convolute result in the formation of magnetic field nulls through which electrons can cross from cathode to anode. The locations of these nulls are illustrated in Figs. 2(b) and 2(c). The simulations model space-charge-limited emission of electrons from cathode surfaces. The emission of electrons is initiated once the local electric field at the surface exceeds 240 kV/cm. This emission-threshold value is consistent with several published estimates for stainless steel and aluminum cathode materials (see, for example, Ref. [34]).

A few test simulations that included the emission of ions (protons) from the anode components were conducted to determine if the presence of positive space-charge in the convolute and *B*-dot probe region would significantly influence the electron energy deposition in the *B*-dot probes. The ion emission model used here is described in detail in Ref. [28]. In the test cases that were considered, no significant changes were found to the electron deposition in the *B*-dot probes when ion emission was included.

To illustrate the complex electron flow in the convolute and MITLs, Fig. 3 plots the electron density in the $\theta = 0$ plane from a simulation at 45 ns. This illustrates the rapid creation and mobility of the electrons throughout the convolute region, especially in the vicinity of the *B*-dot probe aperture. The simulations typically use between 5×10^5 and 1.1×10^6 macroparticles, have a time step $\Delta t \simeq 2.85 \times 10^{-4}$ ns, and run for 1.6×10^5 steps.

The inner-MITL *B*-dot probe designs considered here were modeled as recessed cavities in the upper anode plate. The grid resolution was increased in this region to approximate the significant features of the *B*-dot probes including entrance apertures and cavity wall dimensions. A crude representation of the wire loop is also included in the models, and this provides a relative energy deposition measurement for electron bombardment of the wire loop. Electron energy deposition and scattering in the *B*-dot

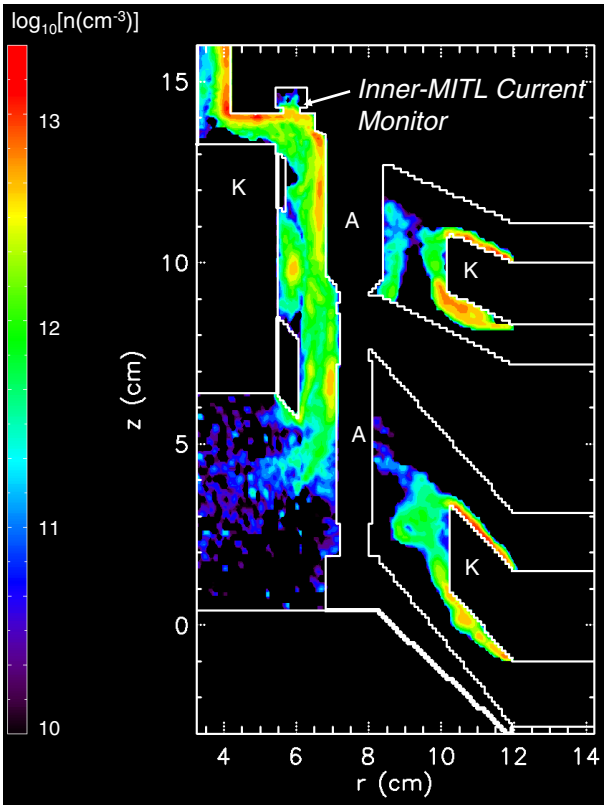

FIG. 3. (Color) Electron density plot illustrating the space-charge power flow in the convolute region with original inner-MITL current probe design at $t = 45$ ns in the $\theta = 0$ plane. Anode (A) and cathode (K) parts are labeled.

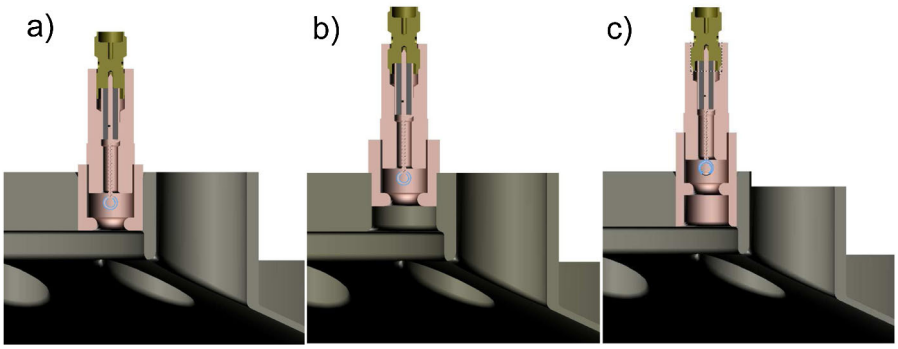

FIG. 4. (Color) Schematic of the (a) original inner-MITL current monitor configuration, (b) the best design, and (c) the experimentally fielded or final design. In each of these schematics, the load is to the left and the upper post of the convolute is to the right of the probe.

probe region is treated using a time-accurate formulation of the Integrated Tiger Series of electron transport Monte Carlo algorithms [35] which are incorporated into LSP [36]. The *B*-dot probe cavity is constructed primarily from copper, and the model includes approximate representations for the thicknesses of cavity walls and apertures.

III. ANALYSIS AND REDESIGN OF THE ORIGINAL *B*-DOT PROBE

The original inner-MITL *B*-dot probe design, which has been used on both the Z and ZR accelerators (see Fig. 6 of Ref. [15]), is shown in Fig. 4(a). The probe is placed immediately downstream of, and in azimuthal alignment with, one of the upper posts to partially shield the probe aperture from electron flow exiting the convolute. The probe contains a single loop of copper wire in the vacuum cavity. The wire has a nominal diameter of 0.404 mm (26 gauge) and is coated with ~0.024 mm of FORMVAR [37] which provides electrical insulation [15]. The two leads are twisted and pass through the top of the vacuum cavity and are attached to a semirigid coaxial cable through which the signal is collected [15]. The wire loop is centered in a 9-mm-diameter copper cavity. The center of the loop is recessed 5.6 mm above the upper-MITL anode surface. The entrance aperture of the probe is 5.1 mm in diameter and 2.5 mm thick. For clarity, we refer to this probe configuration as the *original* design in the remainder of this paper.

The numerical simulations show that the original ZR inner-MITL *B*-dot probe design undergoes electron bombardment before the onset of magnetic insulation of the electron flow. A 3D plot of the particle positions at 30 ns [Fig. 5(a)] shows electrons present in the entrance aperture and cavity. The gray regions in the figure are fabricated from stainless steel; yellow and gold designate copper. The blue particles are electrons launched from the upper cathode on the upstream side of the convolute. The red electrons are emitted from the upper cathode "hole" in the convolute. These electron sources represent the main contributors to the electron energy deposited inside the *B*-dot

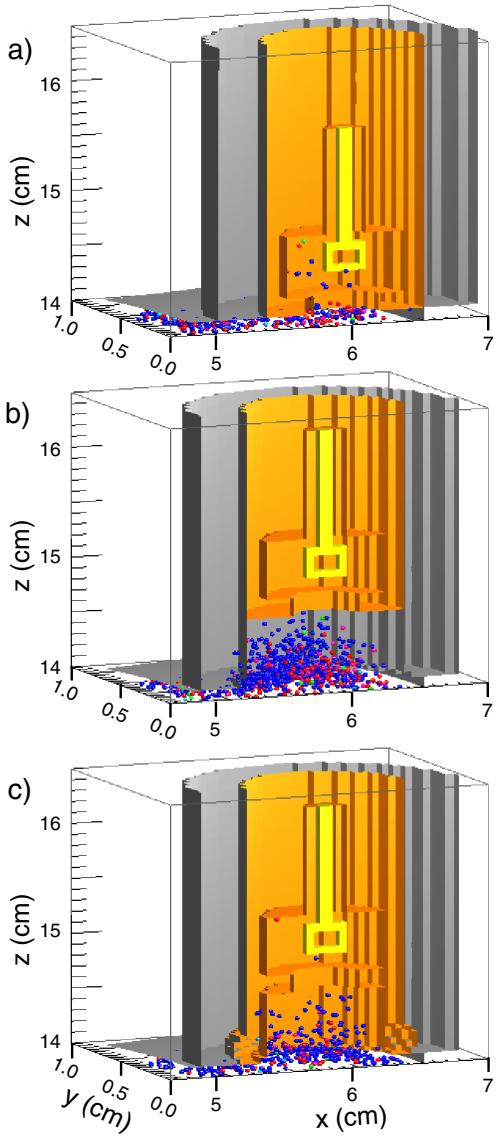

FIG. 5. (Color) Sample particle positions after $t = 30$ ns in simulations of the (a) original inner-MITL *B*-dot probe configuration, (b) the best design, and (c) the final design. The electron macroparticles are colored according to their origin as described in the text.

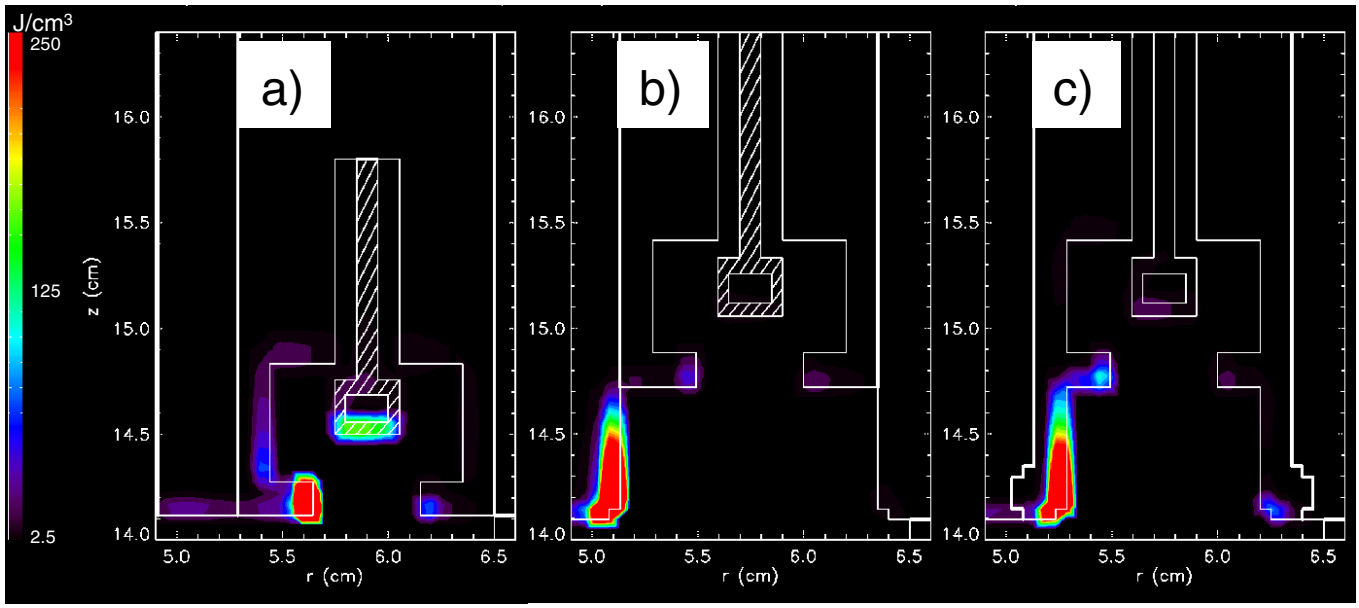

FIG. 6. (Color) Simulated electron energy deposition in the $\theta = 0$ plane after 45 ns for the three inner-MITL *B*-dot probe designs: (a) original, (b) best, and (c) final.

probe cavity and wire loop. Some green particles emitted from the lower cathode components also are visible, but they contribute only a small fraction of the total energy deposited within the probe.

The electron energy deposited in the inner-MITL *B*-dot probe cavity after 45 ns in the $\theta = 0$ plane is shown in Fig. 6(a). Several features immediately stand out. The deposited energy is primarily on the downstream side of the probe cavity. This is because the electrons drift from the convolute towards the load ($-r$ direction) and the magnetic field streamlines have an upward ($+z$ direction) curvature. Note that the color contour levels in Fig. 6 have been truncated at 250 J/cm^3 to facilitate comparison with the other designs. The peak deposited energy (E_{peak}) values for different regions of the probe are given in Table I. The peak deposited energy on the downstream side of the entrance aperture is $\simeq 1.1$ kJ/cm^3. Anode-plasma formation begins at surface temperatures of 400 K [38,39], which corresponds to a deposited energy density of 1.4 kJ/cm^3 in copper. Therefore the peak energy density observed in Fig. 6(a) will likely be sufficient to drive the formation of electrode plasmas. This, in turn, may lead to closure of the aperture on time scales fast enough to impact the current measurement prior to peak load power. In addition, electron energy deposition on the wire after 45 ns has a peak value of $\sim$180 J/cm^3, large enough to suggest that electron strikes to the wire loop might compromise the electrical signal.

TABLE I. Comparison of simulation results for the (a) original, (b) best, and (c) final inner-MITL *B*-dot probe designs. All data from these simulations was taken at 45 ns. The second and fifth columns give the peak deposited energy density (E_{peak}) on the wire loop and the cup aperture, respectively. The third and fourth columns give the total energy deposited (E) on the wire loop and the coaxial wire feed, respectively. The last column gives the magnetic field magnitude ($|B|$) at the center of the wire loop.

Design	E_{peak} Loop (J/cm^3)	E Loop (J)	E Coax/wire (J)	E_{peak} Cup aperture (J/cm^3)	$\|B\|$ Loop center (kG)
(a) Original	189.7	0.89	0.33	1054	20.2
(b) Best	6.9	0.035	0.016	85	7.0
(c) Final	26.5	<0.02	0.028	119	3.9

Based on these findings, we explored a number of options for reducing (i) the energy deposited to the entrance aperture of the cup and (ii) the energy deposited on the wire loop. The design considerations included realistic constraints associated with fielding a probe in the limited space available at the center of the machine, signal-to-noise ratios at the pickup loop, cable connection and routing, and minimization of any modifications to the existing convolute and MITL hardware. The "best" design option that we envisioned was one of the simplest: retraction of the existing *B*-dot hardware assembly approximately 0.6 cm up into the upper anode plate, illustrated in Fig. 4(b). Figure 5(b) shows the simulated retracted probe design and qualitatively illustrates the reduction in the number of electrons present in the *B*-dot cavity. The reduction in the deposited electron energy at the probe entrance aperture and throughout the *B*-dot cavity is shown in Fig. 6(b) (see Table I for peak values). The energy deposited at the inner edge of the hole in the stainless steel anode has a peak deposited energy density

of $\simeq 0.8$ kJ/cm^3, consistent with the results from inside the copper entrance aperture in the original design. However, the effectively larger diameter hole at this peak energy deposition location should reduce the impact of any plasma hole closure on the current measurement.

During the fabrication and calibration stages for this new *B*-dot probe design, the design was modified to include a copper lining of the stainless steel anode hardware. The thickness of this lining was made to be the same as the wall thickness of the inside of the *B*-dot probe cavity. This practical design change provides a more secure fitting for the probe hardware in the finite thickness anode hardware. This change can be seen in Fig. 4(c) and is represented in the simulations by extending the copper wall of the *B*-dot cavity below the copper entrance aperture [see Figs. 5(c) and 6(c)]. We simulated this design change prior to actual testing of the probe on ZR. The main features associated with the improvements of the best design over the original design are mostly retained in the final design (see Table I). The number of electrons that enter the cup prior to the onset of magnetic insulation increases slightly. This increase is reflected by the increased energy deposition on interior walls of the *B*-dot cavity and wire loop (see Table I). The final impact of these design changes relative to the original *B*-dot probe can be seen clearly in Fig. 7 which plots the net electron current entering the 5.1-mm-diameter probe entrance aperture for the three cases. In the original design, electrons striking the inside edge of the entrance aperture can scatter into the probe interior even after the onset of magnetic insulation, keeping the total electron current relatively high. In these simulations, the new designs significantly reduce the electron current entering the probe cavity before the onset of magnetic insulation and effectively eliminate electrons from entering the probe cavity at later times. In the final design, the peak electron current entering the aperture is ~90 A, a reduction by a factor of 6 over the original design.

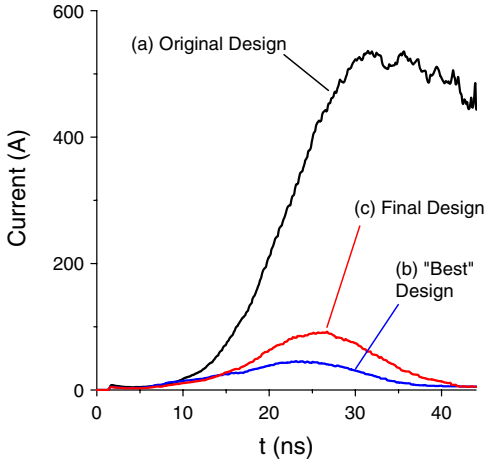

FIG. 7. (Color) The simulated electron current passing through the inner-MITL *B*-dot probe apertures for the (a) original design (black curve), (b) the best design (blue curve), and (c) the final design (red curve) as a function of time.

Table I includes a column for comparing the simulated peak magnetic field magnitude, $|B|$, at the location of the wire loop. It was important to keep this value sufficiently high to permit accurate current measurements in ZR's noisy environment. The values listed in Table I were obtained from simulations that did not include charged particle emission or propagation and did not include the wire loop at the center of the *B*-dot cavity as shown in Figs. 5 and 6. Macroparticle electrons used in the full PIC simulations for determining energy deposition and space-charge currents in the *B*-dot probe typically represent 10^8 to 10^9 actual electrons. Hence, individual particles traveling inside the probe cavity generate large fluctuations in the currents that can disrupt the calculation of the ambient magnetic field inside the probe. Removal of the wire loop in these simulations was also necessary to determine $|B|$ since the simulated wire is much thicker than the 26-gauge copper wire used in the actual probe and therefore tends to largely exclude the ambient magnetic field from the center of the loop. During calibration and fielding of the final probe design, the reduced magnetic field amplitude, measured as a reduced voltage, decreased as predicted by the numerical simulations to within experimental uncertainties.

IV. EXPERIMENTAL RESULTS

The final probe design was fielded on a series of shots that also included the original probe design. For these shots, each of the probes was fielded immediately downstream of one of the 12 upper anode posts, as shown in Fig. 1. Probes of identical design are fielded in opposite polarity pairs, which enables the removal of electron pickup currents from the signals during post-shot data processing [15]. On each of the shots described herein, two each of the original design and two each of the final probe design were fielded. The first test series used relatively low inductance dynamic *z*-pinch loads [40–43] on a series of nominally identical shots. For clarity, we refer to the final probe design as the *redesigned B*-dot probe for the remainder of this paper.

Figure 8 plots the measured MITL current and the average signals from each of the probe designs for two ZR shots, 1951 and 1954. During the rising portion of the power pulse, both *B*-dot designs give the same measured current values which track the outer-MITL current, indicating essentially no current losses between the outer-MITL and inner-MITL *B*-dot probe locations. Near the time of peak power, the MITL current exceeds the load current measured by both probes by an average of ~1.1 MA. For shot 1951, the redesigned probe gives a slightly higher peak load current (the redesigned probe gives 23.3 MA versus 22.8 MA for the original) while for shot 1954, the original probe gives a higher peak load

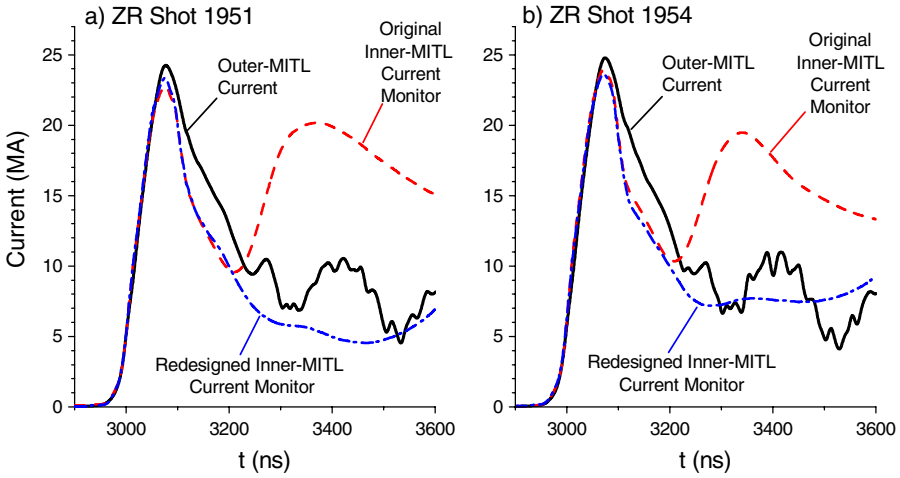

FIG. 8. (Color) Outer-MITL current (solid black line) and inner-MITL load-current measurements from two ZR shots with low-impedance dynamic hohlraum *z*-pinch loads. The current obtained from the original inner-MITL monitor design is shown as a red dashed line and the current obtained from the redesigned inner-MITL monitor is shown as a blue dash-dotted line.

current (the redesigned probe gives 23.6 MA versus 23.9 MA for the original). After peak power, the load currents fall together in good agreement until they reach the ~10-MA level. At this point the original *B*-dot probe currents increase, while the redesigned probe continues to fall and approximately track the MITL current for several hundred ns. This suggests the original *B*-dot probe works well on low-impedance shots through the main power pulse but eventually fails. This failure could arise from either electron current entering the probe as the decreasing load-current results in lower magnetic fields that do not insulate the electron flow from the cup aperture, or from plasma expansion at the probe aperture.

Soft x-rays and UV radiation from these dynamic *z*-pinch loads are a possible mechanism for load-current monitor failure. The dynamic *z*-pinch loads fielded on shots 1951 and 1954 produced approximately 1 MJ of soft x-rays at times near peak load power. Typically load-current monitor failures are correlated only with the time-dependent impedance history of the load. The improved load-current measurement obtained during the rising portion of the power pulse suggests that the failure of the original probe design is not related to photoemission of electrons due to load radiation.

The original and redesigned probes were also fielded on a series of shots with a higher-impedance load. The load was an annular imploding solid liner that was seeded with single-wavelength perturbation features to study the growth of the magneto-Rayleigh-Taylor instability [44,45]. The higher impedance of the load during the rising portion of the power pulse resulted in higher voltages in the MITLs and convolute. The higher voltages result in greater

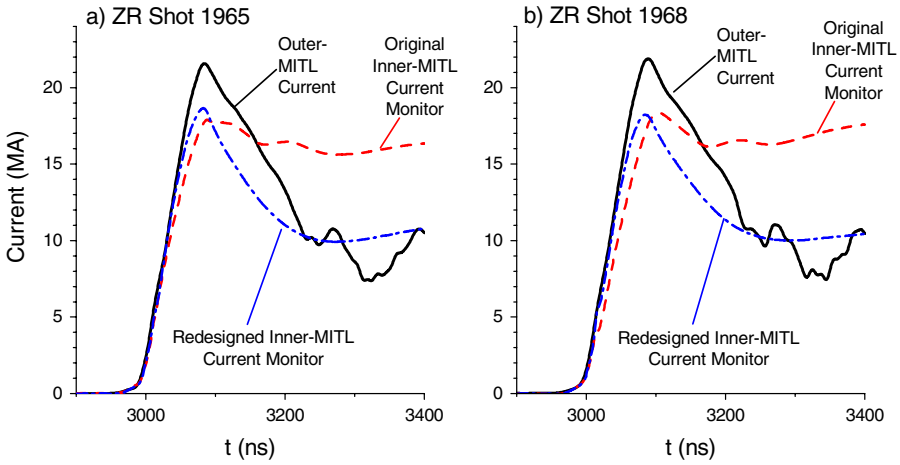

FIG. 9. (Color) Outer-MITL current (solid black line) and inner-MITL load-current measurements from two ZR shots with high-impedance imploding liner loads. The current obtained from the original inner-MITL monitor design is shown as a red dashed line and the current obtained from the redesigned inner-MITL monitor is shown as a blue dash-dotted line.

current losses between the outer-MITL and inner-MITL *B*-dot probes [29]. The actual nature of these current losses is the subject of considerable study [4,14,23–29] with particular emphasis on the formation of electrode plasmas in the convolute that lead to gap closure.

Current measurements from two ZR shots, 1965 and 1968, using identical annular imploding loads are shown in Fig. 9. For both shots, the load current measured by the redesigned *B*-dot probes rises with the MITL until these currents exceed ~15 MA. The original inner-MITL *B*-dot monitor signals begin to deviate from the outer-MITL current during this phase at lower current amplitudes, between 4 MA (shot 1968) and 10 MA (shot 1965). The time-to-peak current value of the redesigned inner-MITL monitors is in good agreement with the outer-MITL current. As in the case of the low-impedance loads, the redesigned inner-MITL *B*-dot monitors give falling current amplitudes that are more consistent with the outer-MITL values at late times. For these liner shots an on-axis 2-mm-diameter tungsten rod was used to quench the x-ray emission from the target to improve the quality of radiographic diagnostic images. As a result, the final inductance of the liner load was probably lower than the final inductance of the dynamic hohlraum load (discussed above), which has a relatively high pinch-convergence ratio. This may explain why the MITL current remains high for a longer period of time on these shots.

We note that these thick metal liner loads produce essentially no x-rays [45], and therefore this potential monitor failure mechanism is not present for shots 1965 and 1968.

V. SUMMARY

Three-dimensional PIC simulations have been used to model the electron power flow in the vicinity of the inner-MITL *B*-dot probe and ZR double-post-hole convolute during the rise time of the power pulse. The simulations show electron energy deposition within the original *B*-dot probe consistent with failure of the probe in relatively high-impedance load shots. New *B*-dot design concepts, inspired by the simulations, have led to a redesign of the inner-MITL *B*-dot probes. These redesigned probes have been fielded simultaneously with the original probes on recent ZR shots. The redesigned probes give current measurements through peak load power for low-impedance shots that are in good agreement with the original probes. In addition, the redesigned probes track the outer-MITL current past the time of peak load power, an improvement over the performance of the original inner-MITL *B*-dot probes. For higher-impedance-load shots, the redesigned probes give load-current rise times that are more consistent with machine current, provide more realistic load-current amplitudes at peak power, and track the machine current well past peak power. Overall, the redesigned inner-MITL *B*-dot probes have proven to be more robust to the deleterious effects of dynamic electron power flow.

The design changes summarized here were guided by large-scale 3D PIC simulations which enabled the rapid evaluation of a number of design ideas. However, the simulations described herein do not address the formation and evolution of *B*-dot aperture plasmas. High-impedance loads generate high voltages inside the MITLs and convolute, which increase the likelihood of rapid formation of dense aperture plasmas early in the pulse. Such plasmas can lead to hole closure, and possibly alter the electron-flow trajectories in the vicinity of the probes. Future work will examine the possible role of electrode plasma formation on inner-MITL *B*-dot probe performance on ZR.

ACKNOWLEDGMENTS

The authors are extremely grateful for the sustained support of this research by J. Porter, K. Matzen, and L. Schneider. We thank K. Androlewicz for providing the rendering of the ZR MITL system in Fig. 1 and M. Dyson for technical editing. Sandia is a multiprogram laboratory operated by Sandia Corporation, a Lockheed Martin Company, for the United States Department of Energy's National Nuclear Security Administration under Contract No. DE-AC04-94-AL85000.

[1] D. H. McDaniel *et al.*, in *Proceedings of the 5th International Conference on Dense Z-Pinches*, edited by J. Davis (American Institute of Physics, New York, 2002), p. 23.

[2] E. A. Weinbrecht, D. D. Bloomquist, D. H. McDaniel, G. R. McKee, G. L. Donovan, J. W. Weed, T. V. Faturos, D. A. Tabor, and C. Moncayo, in *Proceedings of the 16th IEEE Pulsed Power and Plasma Science Conference, Albuquerque, NM, 2007*, edited by E. Schamiloglu and F. Peterkin (IEEE, Piscataway, NJ, 2007), p. 975.

[3] M. E. Savage *et al.*, in Proceedings of the 16th IEEE Pulsed Power and Plasma Science Conference, Albuquerque, NM, 2007 (Ref. [2]), p. 979.

[4] T. D. Pointon, W. L. Langston, and M. E. Savage, in Proceedings of the 16th IEEE Pulsed Power and Plasma Science Conference, Albuquerque, NM, 2007 (Ref. [2]), p. 165.

[5] K. R. LeChien *et al.*, Phys. Rev. ST Accel. Beams **11**, 060402 (2008).

[6] P. A. Corcoran *et al.*, in *Proceedings of the 17th IEEE International Pulsed Power Conference, Washington, DC, 2009*, edited by F. Peterkin and R. Curry (IEEE, Piscataway, NJ, 2009), p. 150.

[7] M. E. Savage and B. S. Stoltzfus, Phys. Rev. ST Accel. Beams **12**, 080401 (2009).

[8] B. Stoltzfus, K. LeChien, M. Savage, and W. Stygar, in Proceedings of the 17th IEEE International Pulsed Power Conference, Washington, DC, 2009 (Ref. [6]), p. 425.

[9] K. LeChien *et al.*, in Proceedings of the 17th IEEE International Pulsed Power Conference, Washington, DC, 2009 (Ref. [6]), p. 604.

[10] K. R. LeChien *et al.*, Phys. Rev. ST Accel. Beams **13**, 030401 (2010).

[11] D. V. Rose *et al.*, Phys. Rev. ST Accel. Beams **13**, 010402 (2010).

[12] D. V. Rose, D. R. Welch, E. A. Madrid, C. L. Miller, R. E. Clark, W. A. Stygar, K. Struve, P. A. Corcoran, and B. Whitney, in *Dense Z-Pinches, 7th International Conference on Dense Z-Pinches*, AIP Conf. Proc. No. 1088, edited by D. A. Hammer and B. R. Kusse (AIP, Alexandria, VA, 2009), p. 263.

[13] J. Lips, J. Garde, A. Owen, R. McKee, and W. Stygar, in Proceedings of the 17th IEEE International Pulsed Power Conference, Washington, DC, 2009 (Ref. [6]), p. 1266.

[14] D. V. Rose *et al.*, in Proceedings of the 17th IEEE International Pulsed Power Conference, Washington, DC, 2009 (Ref. [6]), p. 1153.

[15] T. C. Wagoner *et al.*, Phys. Rev. ST Accel. Beams **11**, 100401 (2008).

[16] D. D. Ryutov, M. S. Derzon, and M. K. Matzen, Rev. Mod. Phys. **72**, 167 (2000).

[17] D. B. Reisman, A. Toor, R. C. Cauble, C. A. Hall, J. R. Asay, M. D. Knudson, and M. D. Furnish, J. Appl. Phys. **89**, 1625 (2001).

[18] M. D. Knudson, C. A. Hall, R. Lemke, C. Deeney, and J. R. Asay, Int. J. Impact Eng. **29**, 377 (2003).

[19] J. R. Asay and M. D. Knudson, in *High-Pressure Shock Compression of Solids VIII: The Science and Technology of High-Velocity Impact*, edited by L. C. Chhabildas, L. Davison, and Y. Horie (Springer, New York, 2005), p. 329.

[20] R. B. Spielman *et al.*, Phys. Plasmas **5**, 2105 (1998).

[21] P. A. Corcoran, J. W. Douglas, I. D. Smith, P. W. Spence, W. A. Stygar, K. W. Struve, T. H. Martin, R. B. Spielman, and H. C. Ives, in *Proceedings of the 11th IEEE International Pulsed Power Conference, Baltimore, MD, 1997*, edited by G. Cooperstein and I. Vitkovitsky (IEEE, Piscataway, NJ, 1997), p. 466.

[22] W. A. Stygar *et al.*, in Proceedings of the 11th IEEE International Pulsed Power Conference, Baltimore, MD, 1997 (Ref. [21]), p. 591.

[23] T. P. Hughes and R. E. Clark, Mission Research Corporation Report No. MRC/ABQ-1875, 1998.

[24] T. P. Hughes and R. E. Clark, Mission Research Corporation Report No. MRC/ABQ-2005, 2000.

[25] T. P. Hughes, R. E. Clark, B. V. Oliver, R. A. St. John, and W. A. Stygar, Mission Research Corporation Report No. MRC/ABQ-2066, 2002.

[26] T. D. Pointon, W. A. Stygar, R. B. Spielman, H. C. Ives, and K. W. Struve, Phys. Plasmas **8**, 4534 (2001).

[27] T. D. Pointon and D. B. Seidel, in Proceedings of the 17th IEEE International Pulsed Power Conference, Washington, DC, 2009 (Ref. [6]), p. 1159.

[28] D. V. Rose, D. R. Welch, T. P. Hughes, R. E. Clark, and W. A. Stygar, Phys. Rev. ST Accel. Beams **11**, 060401 (2008).

[29] W. A. Stygar *et al.*, Phys. Rev. ST Accel. Beams **12**, 120401 (2009).

[30] LSP is a software product developed by ATK Mission Research, Albuquerque, NM 87110, with initial support from the Department of Energy SBIR Program.

[31] C. K. Birdsall and A. B. Langdon, *Plasma Physics via Computer Simulation* (Adam Hilger, New York, 1991).

[32] D. R. Welch, D. V. Rose, M. E. Cuneo, R. B. Campbell, and T. A. Mehlhorn, Phys. Plasmas **13**, 063105 (2006).

[33] D. R. Welch, D. V. Rose, N. Bruner, R. E. Clark, B. V. Oliver, K. Hahn, and M. Johnston, Phys. Plasmas **16**, 123102 (2009).

[34] M. S. Di Capua and D. G. Pellinen, J. Appl. Phys. **50**, 3713 (1979).

[35] J. A. Halbleib, R. P. Kensek, G. D. Valdez, S. M. Seltzer, and M. J. Berger, IEEE Trans. Nucl. Sci. **39**, 1025 (1992).

[36] D. V. Rose, D. R. Welch, B. V. Oliver, R. E. Clark, D. L. Johnson, J. E. Maenchen, P. R. Menge, C. L. Olson, and D. C. Rovang, J. Appl. Phys. **91**, 3328 (2002).

[37] FORMVAR is a product of MWS Wire Industries, Westlake Village, California, USA, www.mwswire.com.

[38] A. E. Blaugrund, G. Cooperstein, and S. A. Goldstein, Phys. Fluids **20**, 1185 (1977).

[39] T. W. L. Sanford *et al.*, J. Appl. Phys. **66**, 10 (1989).

[40] T. W. L. Sanford *et al.*, Phys. Plasmas **9**, 3573 (2002).

[41] J. E. Bailey *et al.*, Phys. Plasmas **13**, 056301 (2006).

[42] S. A. Slutz *et al.*, Phys. Plasmas **13**, 102701 (2006).

[43] G. A. Rochau *et al.*, Plasma Phys. Controlled Fusion **49**, B591 (2007).

[44] D. Sinars, S. Slutz, M. Herrmann, K. Peterson, R. Vesey, and B. Blue, Bull. Am. Phys. Soc. **54**, 100 (2009), http://meetings.aps.org/Meeting/DPP09/Event/109074.

[45] S. A. Slutz, M. C. Herrmann, R. A. Vesey, A. B. Sefkow, D. B. Sinars, D. C. Rovang, K. J. Peterson, and M. E. Cuneo, Phys. Plasmas **17**, 056303 (2010).